Photodissociation of the trichloromethyl radical: photofragment imaging and femtosecond photoelectron spectroscopy

Christian Matthaei, Deb Pratim Mukhopadhyay, Anja Röder, Lionel Poisson, Ingo Fischer

Photodissociation of the Trichloromethyl Radical: Photofragment Imaging and Femtosecond Photoelectron Spectroscopy

Christian T. Matthaei[a], Deb Pratim Mukhopadhyay[a,b], Anja M. Röder[a,c,d], Lionel Poisson[c], Ingo Fischer[a,*]

Halogen-containing radicals play a key role in catalytic reactions leading to stratospheric ozone destruction, thus their photochemistry is of considerable interest. Here we investigate the photodissociation dynamics of the trichloromethyl radical, CCl_3 after excitation in the ultraviolet. While the primary processes directly after light absorption are followed by femtosecond-time resolved photoionisation and photoelectron spectroscopy, the reaction products are monitored by photofragment imaging using nanosecond-lasers. The dominant reaction is loss of a Cl atom, associated with a CCl_2 fragment. However, the detection of Cl atoms is of limited value, because in the pyrolysis CCl_2 is formed as a side product, which in turn dissociates to CCl + Cl. We therefore additionally monitored the molecular fragments CCl_2 and CCl by photoionisation at 118.2 nm and disentangled the contributions from various processes. A comparison of the CCl images with control experiments on CCl_2 suggest that the dissociation to CCl + Cl_2 contributes to the photochemistry of CCl_3.

A Introduction

The photochemistry of halogen-containing species has gained considerable interest since the discovery of their role in the destruction of stratospheric ozone.[1] Numerous alkyl and alkenyl halides, in particular chlorine-substituted have thus been investigated in the gas phase over the years to obtain UV photoabsorption and photodissociation cross sections, but also photodissociation products and branching ratios.[2-9] In contrast, much less is known about open-shell species, i.e. chloroalkyl radicals. Diatomics CX (X=F, Cl, Br, I) have been investigated by high-resolution spectroscopy and their excited states were characterized in detail.[10, 11] The electronic spectroscopy of CCl_2 has been studied in matrix[12] as well as in the gas phase.[13, 14] The photodissociation of CCl_2 to CCl + Cl has been explored by the Daggidian group using laser-induced fluorescence, who reported both the spin-orbit branching ration of Cl as well as a bimodal rotational state distribution of CCl,[15-17] and by Huber and coworkers, who applied photofragment translational spectroscopy.[18] Also the excited states of mixed carbenes CXY were characterized by high resolution electronic spectroscopy.[19-22]

Here we focus on the trichloromethyl radical, CCl_3, which appears as an intermediate in the photodissociation of chloroalkanes and -alkenes in the upper atmosphere,[23, 24] compounds that are involved in stratospheric ozone depletion. The kinetics of the $CCl_3 + O_2$ reaction has also been monitored because of its relevance in plasma etching.[25-27] UV absorption and multiphoton ionisation (MPI) yielded information on two-photon excited Rydberg states.[28] Danis et al. identified a structureless band with maximum absorption at 210 nm and an absorption cross section σ_{abs} =14.5 Mb.[29] This band was later assigned to the transition from the X $^2A_1$ ground state into the C $^2A_1'$ (3s) Rydberg state.[30] Partial resolution of the out-of-plane bending mode and absorption cross sections σ_{abs} at the band heads ranging from 10.2 Mb at 224.8 nm to 1.7 Mb at 250.5 nm were reported, in qualitative agreement with the previous work. An accurate ionisation energy (IE) of 8.06 eV as well as information on the ionic ground state was obtained from a vibrationally resolved photoelectron spectrum.[31] While the neutral ground state is pyramidal (C_{3v}) the ionic ground state is planar (D_{3h}). However, the excited state dynamics has been scarcely explored. The only experimental study of Hintsa et al. used translational energy spectroscopy to explore the photodissociation at 308 nm.[32] In this work, only loss of chlorine was found, thus the dominant photodissociation pathway is $CCl_3 \rightarrow CCl_2 + Cl$. Hintsa et al reported an average translational energy release of 13 kcal·mol^{-1} (54 kJ·mol^{-1}) and an anisotropy parameter $\beta \approx 1 \pm 0.2$. Computationally, the neutral and ionic ground state have been investigated,[31, 33] but information available on the excited electronic states is limited to low-level methods like Hartree-Fock.[28] In order to obtain a full picture of the excited-state dynamics of CCl_3, we initiated a study that combines femtosecond-time resolved photoionisation and photoelectron spectroscopy (TR-PES) [34-36] to explore the initial processes following photoexcitation with nanosecond photofragment imaging[37, 38] to

[a] Institute of Physical and Theoretical Chemistry, University of Würzburg, Am Hubland, D-97074 Würzburg, Germany, e-mail: ingo.fischer@uni-wuerzburg.de
[b] Present address: Department of Dynamics of Molecules and Clusters, J. Heyrovský Institute of Physical Chemistry, Dolejškova 2155/3, 182 23 Praha 8, Czech Republic
[c] LIDYL, CEA, CNRS, Université Paris-Saclay, CEA Saclay 91191 Gif-sur-Yvette France, e-mail: lionel.poisson@universite-paris-saclay.fr
[d] Present address: Max-Born-Institute for Nonlinear Optics and Short Pulse Spectroscopy, Max-Born-Straße 2 A, D-12489 Berlin, Germany

Electronic Supplementary Information (ESI) available: [details of any supplementary information available should be included here]. See DOI: 10.1039/x0xx00000x

monitor the photodissociation products. The latter approach has evolved into a method that provides detailed insight into the photodissociation mechanism of stable molecules[38-40] and radicals[41] by monitoring the translational energy release of photofragments. In the past, we applied the method to investigate H-atom loss from radicals,[42] biradicals[43] and carbenes,[44] but recently extended our work to chlorine-containing molecules.[45] Experiments are accompanied by computations using time-dependent density functional theory (TD-DFT).

B Experimental

CCl_3 was generated by flash pyrolysis either from CCl_3Br or from CCl_4. In addition, $CHCl_3$ (chloroform) was employed for control experiments on CCl_2. All precursors were commercially obtained from Sigma-Aldrich, seeded in around 1.5 - 2 bar of Ar and thermally cleaved in an electrically heated SiC tube, mounted on a solenoid pulsed valve. In the subsequent adiabatic expansion, the radicals are typically cooled to vibrational temperatures of 150 K, as concluded from previous work.[43]

In both, the femtosecond (fs-) time resolved experiments and the nanosecond (ns-) photofragment detection, the velocity map imaging (VMI) technique was applied.[37, 38] Fs-time resolved experiments were conducted at the LUCA/SLIC laser facility. Photoelectron images (PEI) were recorded and yielded the TR-PES. Experimental conditions were similar to previous experiments.[46, 47] Briefly, the tripled fundamental of the Ti:Sa laser around 266 nm (10-50 μJ) was used as the pump pulse, for the probe pulse the fundamental of the Ti:Sa laser (798 nm, 0.1-0.7 mJ) was employed. For the time-resolved mass spectra six scans were averaged, for the photoelectron images seven scans. Within one scan the ion signal as well as the PE images were integrated over 150 laser shots. As no dependence on the relative polarisation of the pump and probe pulses was observed, the rotational mean is discussed in the experimental spectra. The one-colour background signal was subtracted from the delay traces. The ns-experiments were conducted at the University of Würzburg, using a photofragment imaging setup.[42, 45] A skimmed free molecular jet enters the time of flight mass spectrometer (TOF-MS), which can be operated in either space-focusing or VMI configuration. Two separate counterpropagating ns-laser systems were used to dissociate and ionize the fragments. For photodissociation, the unfocused frequency-doubled output of a Nd:YAG laser pumped dye laser (230 nm – 250 nm/5.39 eV - 4.96 eV) with 0.5-1.0 mJ/pulse was used, polarized parallel to the detector plane. For ionisation we either employed the 9th harmonic of a Nd-YAG laser at 118.2 nm for the molecular fragments or a second tuneable dye laser system for ionisation of Cl atoms in a [1+1'] resonance-enhanced MPI process. In the latter, the $^2D_{5/2} \leftarrow {}^2P^o_{3/2}$ transition of Cl was excited by 118.9 nm radiation, produced by frequency tripling the second harmonic output of a second dye laser system in Xe. Note that the spin-orbit excited $^2P_{1/2}$ state of Cl cannot be probed by this scheme, as discussed previously, because there is no suitable transition in the tripling range accessible with the setup.[45]

For these experiments, the dye laser was scanned over the entire Doppler profile of the atomic transition. The residual 356.7 nm light was employed for the ionisation step.[45] The velocity map images were accumulated over 10^4 laser shots and one-colour background was subtracted. Mass spectra were recorded by monitoring the current generated upon ion impact on the MCPs. Further details on the ion optics, the imaging detector and the laser systems are given in the ESI.

In both fs-PEI and ns-photofragment imaging, the 3D Newton sphere was reconstructed from the image via inverse Abel transformation with the pBASEX algorithm, employing Legendre polynomials up to the 4th order.[48] From this reconstruction, the photoelectron spectra (fs-experiments) and the translational energy release distributions $P(E_T)$ (ns-experiments) were derived.

Calculations were performed using DFT (density functional theory) employing the Qchem4 package, the CAM-B3LYP functional and the aug-cc-pVTZ basis set.[49] Excited states were calculated using TD-DFT, also employing the CAM-B3LYP functional and the aug-cc-pVTZ basis set. TD-DFT is rather simple and inexpensive method that nevertheless yields reasonably accurate vertical excitation energies for many radicals.[50] Spin contamination can be problematic, but were negligible in the computations presented below. For all calculated states, S^2 was around 0.8 at most, with a nominal value of 0.75.

C Results

Calculations

The CCl_3 radical is C_{3v}-symmetric with a X $^2A_1$ electronic ground state. For the optimized ground state structure, we find a C-Cl bond length $R_{C\text{-}Cl}$ = 1.708 Å, and angles $\alpha_{Cl\text{-}C\text{-}Cl}$= 117.3° and $d_{Cl\text{-}C\text{-}Cl\text{-}Cl}$= -148.0°, in agreement with previous work.[31] The singly occupied molecular orbital (SOMO) can be seen in a first approximation as a *p*-orbital centred at the carbon atom, with contributions from the non-bonding orbitals at the chlorine. The relevant excited states, as well as vertical excitation energies and oscillator strengths for transitions from the ground state, as well as an approximate character of the transition are given in Table 1.

Table 1: Vertical excitation energies (at the ground state minimum geometry) and oscillator strengths f, computed by TD-DFT.

State	E_{vert} /eV	Osc. Strength *f*	Attribution
2 $^2A_1$	3.80	$9.1\cdot10^{-5}$	SOMO→LUMO, (C-Cl antibonding)
1 $^2A_2$	4.96	0	$n_{Cl} \rightarrow$ SOMO
1 ^2E	5.41	$4.1\cdot10^{-5}$	SOMO → 3*p*-Rydberg/ HOMO-2 → SOMO
2 ^2E	5.69	$4.2\cdot10^{-2}$	HOMO-2 → SOMO
3 $^2A_1$	5.74	$1.3\cdot10^{-2}$	SOMO →3*s*-Rydberg

The transition into the lowest-lying excited state is centred in the near UV at 3.80 eV, corresponding to 326 nm. With an oscillator strength *f* around 10^{-4} it is expected to be rather weak. The second excited state is of A_2 symmetry, thus transitions from the ground state are dipole-forbidden. Above 5 eV a number of close-lying excited states are computed, two of them with considerable Rydberg character. Due to their energetic proximity the states are expected to be strongly coupled. Transitions into the 1 ^{2}E state are again expected to be rather weak. The next states, the 2 ^{2}E and the 3 $^2A_1$ (3s) state are associated with f=0.1-0.01 and thus provide the absorption strength for excitation in the far-UV. In previous work an absorption band was observed that sets in around 270 nm and maximises at 210 nm, corresponding to E_{vert} =5.90 eV. It has been assigned to the 3 $^2A_1$ (3s) state ($^2A_1$' in D_{3h}).[30] The computed transition dipole moment μ_T is oriented along the symmetry axis of the radical. Based on our computations, the 2 ^{2}E will also contribute to this band. Here, μ_T is perpendicular to the symmetry axis. From a comparison with the experimental work we conclude that the computed E_{vert} are accurate to within ±0.2 eV.

Mass Spectra

Figure 1a) shows the two-colour photoionisation mass spectrum (PIMS) of pyrolysed CCl_4 with 230 nm excitation and 118.2 nm ionisation (black line). Note that CCl_4 has an IE of 11.47 eV, thus no signal was observed without pyrolysis. A power of 40 W was applied to the SiC tube, corresponding to roughly 700 - 800 K. The main pyrolysis product is CCl_3 (m/z = 117-123), contributions from CCl_2 (m/z 82-86) and CCl (47, 49) are also identified. Minute amounts of C_2Cl_2 (m/z 94- 98), C_2Cl_3 (m/z 129-135) and C_2Cl_4 (m/z 164- 172) can also be observed. Close ups of the relevant contributions CCl, CCl_2 and CCl_3 are shown in Figure 1b), c) and d). The red and blue curves represent the signals with only ionisation or dissociation laser present. Upon turning the dissociation laser on, the CCl and CCl_2 signals increases roughly by a factor of two (black curve), indicating that they are formed in the dissociation, while the CCl_3 signal stays constant within the accuracy of the experiment. Also, one-colour ionisation of CCl by the 230 nm radiation is visible. Due to the delay between the two lasers, the peak appears at earlier time-of-flight, corresponding to m/z 38 and 40 for the two-colour signal. PIMS were also recorded at 235 nm, 240 nm, 245 nm and 250 nm. In agreement with the reported absorption cross section of CCl_3 the two-colour signal decreases with increasing wavelength.[30] Mass spectra using chloroform as a precursor are given in Figure S1 in the Electronic Supplementary Information (ESI). As expected from previous work, they show CCl_2 to be the dominant pyrolysis product.[17, 51] Typical mass spectra obtained in the femtosecond experiments using CCl_3Br with pyrolysis present (black line) and without pyrolysis (red line) are given in Figure 2. They were recorded with pump- and probe-laser present at around time zero. While the mass spectrum without pyrolysis shows no appreciable signal at all, an intense signal corresponding to CCl_3 appears with active pyrolysis. Small mass peaks due to Br (m/z 79/81) and CCl_2 as well as C_2Cl_4 (m/z 164-172) are visible. Mass spectra with pump- and probe-laser only revealed a one-colour background signal that was at least a factor of ten smaller than the pump-probe signal. Note that we stopped using CCl_3Br in the ns-experiments, because the presence of several mixed radicals CCl_xBr that were efficiently excited at shorter wavelengths complicated data interpretation.

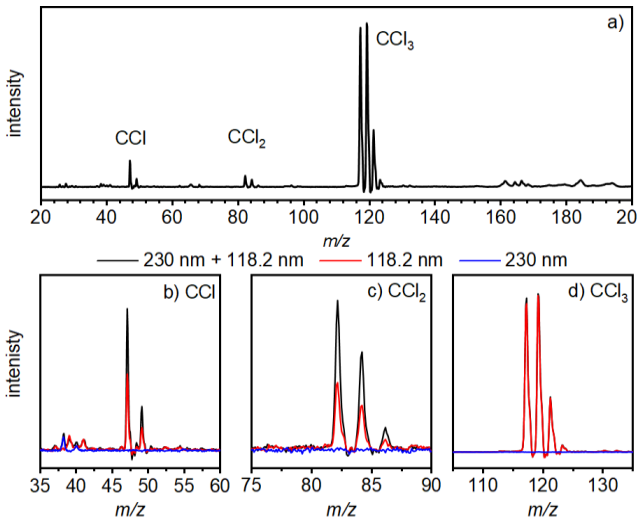

Figure 1: In a) the two-colour mass spectrum using CCl_4 as a precursor recorded with 230 nm dissociation and a 118.2 nm ionisation wavelength is shown. Below, close-ups of the b) CCl , c) CCl_2 and d)CCl_3 mass signals are displayed. In red the signal generated by only the ionisation laser and in blue by only the dissociation laser are shown. As visible, CCl and CCl_2 signals increase in the two-colour process. For CCl, a one-colour signal caused by the 230 nm radiation alone is present. Due to the delay between the two lasers it appears in the same region as the two-colour signals of m/z 38 and 40.

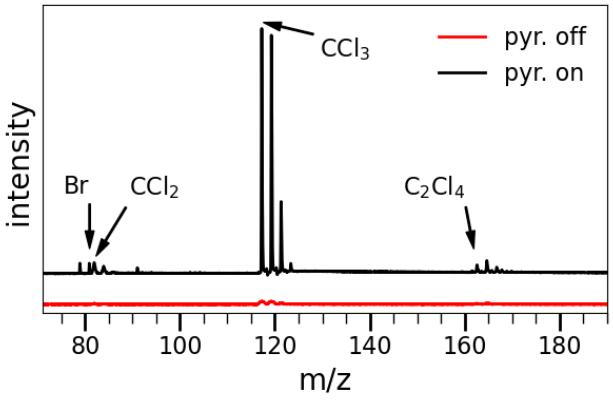

Figure 2: Mass spectra with and without pyrolysis, recorded with fs-lasers, λ_{pump} = 266 nm and λ_{probe} = 798 nm around time zero. CCl_3Br was employed as a precursor.

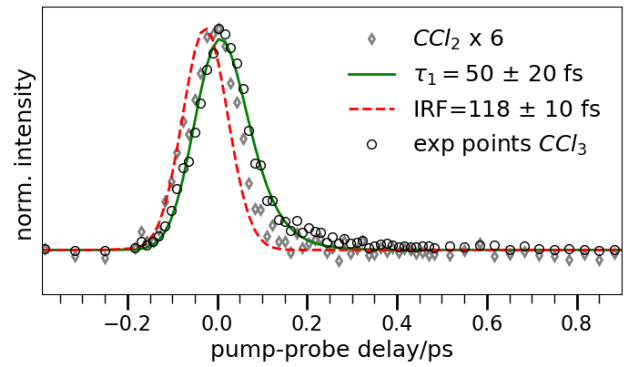

Figure 3: The time-resolved ion signal of CCl_3 (open circles) at 266 nm excitation is fitted by a monoexponential decay with a time constant of 50 fs. As visible, the fit underestimates the signal intensity beyond 200 fs, indicating the presence of a second contribution. For comparison, the CCl_2 signal (signal multiplied by six for ease of viewing) and the instrument response function (dashed red line) are given.

Time-resolved experiments

To investigate the primary photophysical processes in CCl_3 directly after excitation we conducted fs-time-resolved experiments, using ion and photoelectron detection. In Figure 3 the time-resolved ion signal is depicted. The CCl_3 signal (open circles) decays quickly and a monoexponential fit (green line) yields a time constant of 50±20 fs. The instrument response function (IRF) of 118±10 fs employed in the fit is given as a dashed red line for comparison and shows that despite the short lifetime a reliable time constant can be extracted. At longer delay times the fit consistently underestimates the signal intensity, which indicates the presence of a second time constant on the order of 100 -150 fs. However, an accurate value cannot be determined, because the contribution to the signal is too low.

As discussed above, TR-PES provides additional information not available from the mass spectra, albeit at the cost of losing mass information. Thus, possible side products from the pyrolysis have to be considered. We therefore included the time-dependent ion signal of the most relevant side product CCl_2 in Figure 3 (open diamonds). The signal was multiplied by a factor of six for a better comparison. As visible, the signal deviates only slightly from the IRF, thus the lifetime is significantly shorter than 50 fs. In addition, the signal has disappeared beyond 150 fs.

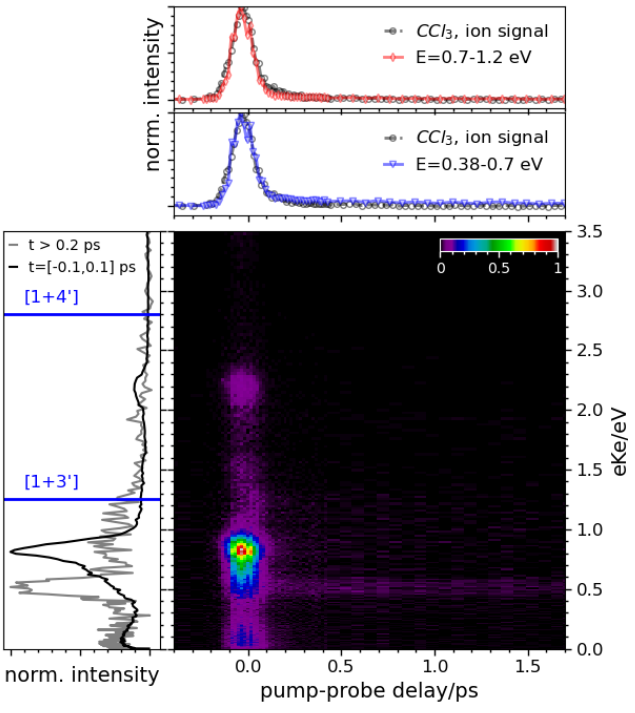

Figure 4: TR-PES spectrum with 266 nm pump/798 nm probe, displayed as a 2D-map. In the top trace the time-dependence of the photoelectron signal at two selected energy ranges is depicted and compared to the decay trace of CCl_3 ion signal obtained from the mass spectra (grey open circles). The graph on the left shows the photoelectron kinetic energy summed over all delay times. The trace for t>0.2 ps has been scaled for ease of viewing. The average signal collected before the t_0 was subtracted from the whole signal.

In Figure 4 the time-resolved photoelectron spectrum is displayed as 2D map. Although CCl_3 dominates the mass spectrum (Figure 2), small contributions from side products are present and have to be taken into account. At an electron kinetic energy (eKE) of 0.5 eV (left-hand panel) a time-dependent signal without observable decay is visible. Note that the trace for t>0.2 ps has been scaled for ease of viewing. An ion signal with the same time-dependence is observed for Br (see Figure S2), therefore we assign the signal to bromine atoms formed in the pyrolysis.[#)] The photoelectron signal from CCl_3 itself starts at around 1 eV, trailing to lower kinetic energies. Taking the IE of 8.06 eV into account,[31] the eKE confirms ionisation in a [1+3'] process with a total photon energy of around 9.32 eV. Two-photon excitation in the pump step can thus be excluded based on the energetics. Thus we are certain that the UV-absorption band reported by Ellermann is indeed excited, although 266 nm is close to the red edge of the band.[30] The shoulder to lower eKE represents transitions into vibrationally excited states of the ion that cannot be resolved due to the laser bandwidth. The vibrational envelope appears due to the large geometry change upon ionisation. A very small signal at 2.3 eV represents an [1+4'] ionisation contribution. For CCl_2 an IE of 9.27 eV was determined,[51] thus only transitions with low eKE are expected. Indeed, a peak close to 0 eV and only present around t_0 can be recognized in the 2D map. We therefore assume, that the electron signal above 0.7 eV does only contain contributions from CCl_3. The time-delay traces above the 2D map show the electron signal averaged over two ekE ranges (blue and red lines). The top one (0.7-1.2 eV, red line) is indeed almost identical to the CCl_3 ion signal and yields the same time constant. The lower trace, averaged over the kinetic energies from 0.38 to 0.7 eV (blue line) contains contributions from Br and is offset at late times compared to the ion signal due to the resonant ionisation of bromine atoms.

Nanosecond Photofragment Imaging

Photofragment imaging of CCl_3 photodissociation. In the next step, the UV photodissociation of CCl_3 has been investigated between 230 nm (520.1 kJ·mol^{-1}/5.39 eV) and 250 nm (478.5 kJ·mol^{-1}/4.96 eV). In this region, two product channels are accessible, loss of a Cl atom (I) and loss of Cl_2 (II). The reaction pathways are depicted in Scheme 1. Note that CCl_2 can be formed in its singlet ground state or the first excited triplet state.

$CCl_3 \rightarrow CCl_2 (X\ ^1A_1) + Cl\ (^2P_{3/2})$ $\quad \Delta_R H° = 280$ kJ·mol^{-1} (Ia)

$CCl_3 \rightarrow CCl_2 (a\ ^3B_1) + Cl\ (^2P_{3/2})$ $\quad \Delta_R H° = 365$ kJ·mol^{-1} (Ib)

$CCl_3 \rightarrow CCl\ (X\ ^2\Pi) + Cl_2\ (X\ ^2\Pi)$ $\quad \Delta_R H° = 363$ kJ·mol^{-1} (II)

Both (Ia) and (Ib) can also be formed in conjunction with the spin-orbit excited $^2P_{1/2}$ state of Cl (+0.109 eV/10.52 kJ·mol^{-1}). The first excited (open-shell) singlet state is at +17265 cm^{-1} above the ground state (+206 kJ/mol) and thus barely accessible at the highest excitation energies.[13] It is therefore neglected in the analysis below.

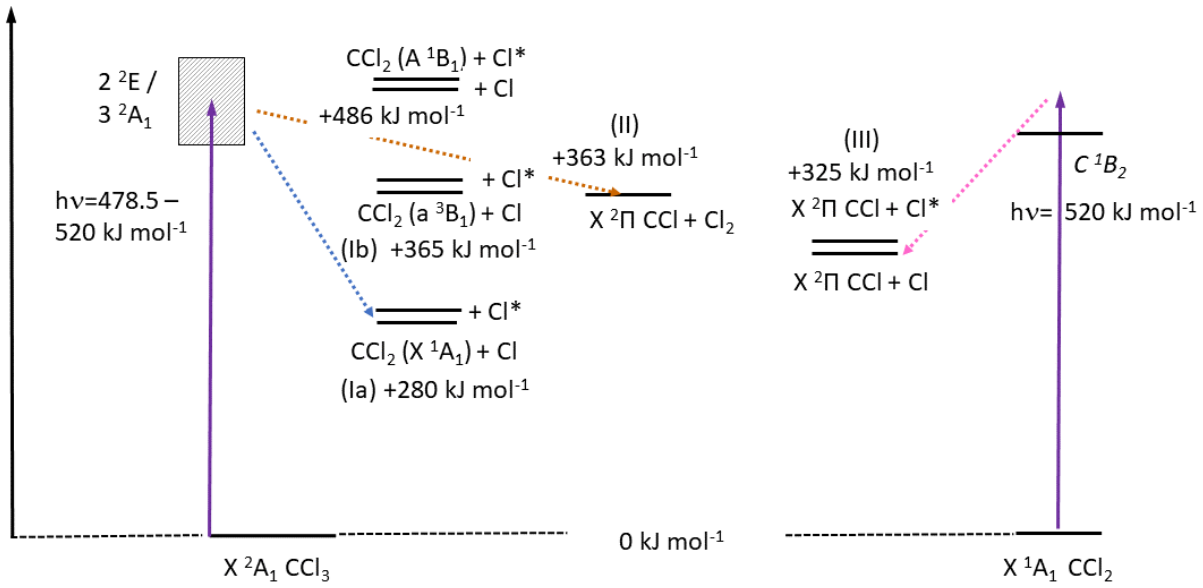

Scheme 1. Summary of the relevant dissociation pathways in CCl_3 (left-hand side) and CCl_2 (right-hand side). The major product of CCl_3 photodissociation is dichlorocarbene in its X $^1A_1$ ground state (blue line). Loss of Cl_2 seems to be present as well (brown line). CCl_2 is also formed in the pyrolysis and dissociates to CCl + Cl (magenta line).

Heats of reaction were computed from data given in the Active Thermochemical Tables (ATcT).[52, 53] For comparison, we computed $\Delta_R H°(0K)$ = 278 kJ mol^{-1} for (Ia). We assume that only a negligible reverse barrier is present, so $\Delta_R H°$ is approximated to the bond dissociation energy, BDE. Formation of CCl in conjunction with two chlorine atoms is thermochemically not possible upon one-photon excitation. Nevertheless, photodissociation of CCl_2 has to be considered in the analysis, because it is produced as a further pyrolysis product (see Figure 1 and Scheme 1) and dissociates after single photon absorption (III).

$$CCl_2\ (pyro) \xrightarrow{+h\nu} CCl + Cl \qquad \Delta_R H° = 325\ kJ{\cdot}mol^{-1} \qquad (III)$$

Alternatively, CCl_2 generated in the photodissociation of CCl_3 can dissociate after absorption of a second photon (IV), corresponding to two-photon dissociation of CCl_3.

$$CCl_3 \xrightarrow{+h\nu} CCl_2\ (photo) + Cl \xrightarrow{+h\nu} CCl + 2\ Cl \qquad (IV)$$

Note that CCl_2 (photo) generated in (Ia) or (Ib) will store part of the excess energy in the vibrational and rotational degrees of freedom, whereas CCl_2 (pyro) will be cooled in the jet expansion.

The CCl_4 precursor can also lose Cl or Cl_2, but the tabulated absorption cross sections at 298 K lie between 0.02 Mb at 230 nm and 10^{-3} Mb at 250 nm, two to three orders of magnitude smaller than those of CCl_3.[54] Indeed, we did not observe any photodissociation from pure CCl_4 without pyrolysis. Nevertheless, vibrational excitation acquired in the pyrolysis might increase the photodissociation cross section. It should also be kept in mind that CCl_4 is not observable in the mass spectrum and the pyrolytic conversion is thus unclear. Therefore, we will consider its thermochemistry as well.

$$CCl_4 \rightarrow CCl_3 + Cl\ (^2P_{3/2}) \qquad \Delta_R H° = 288\ kJ\ mol^{-1} \qquad (V)$$

$$CCl_4 \rightarrow CCl_2 + Cl_2 \qquad \Delta_R H° = 326\ kJ\ mol^{-1} \qquad (VI)$$

While most experiments on CCl_4 were conducted in the VUV range, Kawasaki et al investigated the photodissociation in a one-colour experiment at 235 nm (509 kJ·mol^{-1}) and found a Cl/Cl* ratio of 8/2, with a Boltzmann-type distribution for Cl.[55] However, the large translational energy release of the Cl* atoms that extends to more than 40 kcal·mol^{-1} (167 kJ·mol^{-1}) indicates the presence of a contribution from multiphoton excitation. For (VI) a quantum yield of only 5% was found at 214 nm,[56] compared with >90% for (V), with its relative importance increasing towards higher excitation energies (i.e. decreasing to longer wavelengths).

In general, an image of the atomic fragment of a photodissociation, in this case Cl, is simpler and easier to interpret. However,

from the presence of Cl in (I), (III), (IV) and possibly (V) a superposition of several contributions is expected, and the additional detection of the molecular fragment is required. Therefore, in a first series of experiments, images of the CCl_2 photoproduct ionized at 118.2 nm were recorded. Due to the subtraction of one-colour background signals, CCl_2 generated in the pyrolysis does not contribute to the image. Formation of CCl_2 from CCl_4 via (VI) is neglected, due to the small quantum yield observed at 214 nm and the even lower one expected at 230 nm. Translational energy distributions $P(E_T)$ probing CCl_2 upon 230 nm (upper trace, blue) and 250 nm excitation (lower trace, red) are given in Figure 5. The reconstructed image is visible on the right hand side. Experiments were also performed at 235 nm, 240 nm and 245 nm under the same conditions, the data are displayed in Figure S4. Note that throughout the paper we plot E_T of the respective fragment rather than the total translational energy release, because in the analysis, contributions from several molecules have to be included and compared. Excitation at 266 nm was also used for better comparison with the fs-data, but the photofragment signals beyond 250 nm were small and difficult to separate from the background signals.

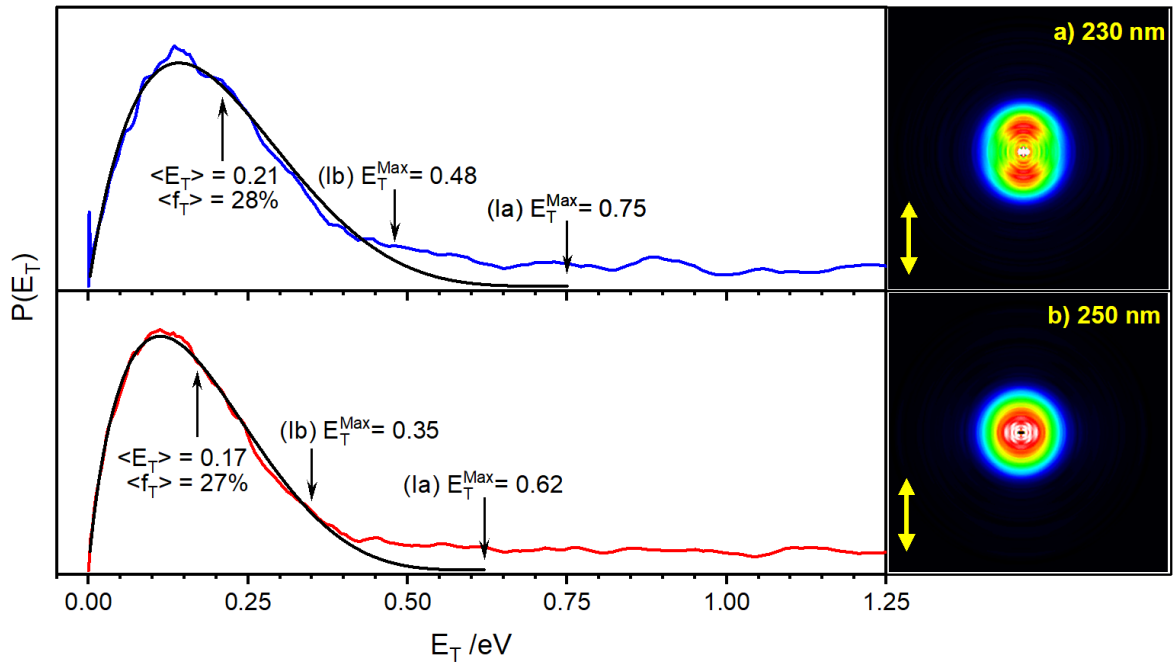

Figure 5: Translational energy distribution $P(E_T)$ of the CCl_2 fragment upon excitation with a) 230 nm and b) 250 nm light. The experimental results are drawn in blue and red respectively and a fit using expression (1) in black. The corresponding velocity map images are shown with a yellow arrow indicating the laser polarisation. Note that only the translational energy of the CCl_2 fragment is plotted on the abscissa. $\langle E_T \rangle_{total}$ amounts to 0.70 eV at 230 nm and 0.57 eV at 250 nm.

A unimodal energy distribution is observed with a shape that is independent of the dissociation wavelength. At both wavelengths, a background is visible that extends over all translational energies. The images on the right-hand side show a small anisotropy in the fragment distribution, which indicates a fast dissociation in less than a rotational period. The photofragment angular distributions (PAD) are given in Figure S6. From the PAD a value for the anisotropy parameter β of 0.5, is extracted at 230 nm, which decreases to around β = 0.06 at 250 nm.

As in previous work an empirical two-parameter function was used to fit the experimental data and extract the expectation value for the translational energy release, $\langle E_T \rangle$. [57-59]

$$\boldsymbol{P(E_T) = C(E_T)^a\,(E_T^{max} - E_T)^b} \qquad (1)$$

Here *C* is a normalisation constant, *a* and *b* are the two fitting constants and $\boldsymbol{E_T^{Max}}$ is the maximum available translational energy for the fragment upon photodissociation, computed from (2) and indicated by arrows in the Figure.

$$\boldsymbol{E_T^{max}(A) = \frac{m_B}{m_{A-B}}(h\nu - BDE)} \qquad (2)$$

This fit is used for extracting the expectation value from the recorded data. As an example, fitting the experimental data at a dissociation wavelength of 230 nm with the two-parameter fit results in an expectation value for the fraction of excess energy released as translation, $\boldsymbol{\langle f_T \rangle = \langle E_T \rangle / E_T^{max}}$ = 28%, assuming channel (Ia), i.e. formation of CCl_2 in its electronic ground state. As visible in particular for 250 nm (lower trace), $P(E_T)$ extends beyond the cut-off expected for formation of CCl_2 in the excited triplet state, so (Ib) is considered to be of minor importance. Note that the spin-orbit splitting in Cl is 881 cm^{-1} (0.109 eV) and cannot be resolved in the data. Also product vibrations are not resolved. A summary of the values obtained at the various dissociation wavelengths is shown in Table 2.

The anisotropic photofragment angular distribution indicates a dissociation that proceeds faster than a rotational period, i.e. along a repulsive coordinate. The expectation value of such a direct dissociation can be calculated with an impulsive model described by Tuck[60] and by Galloway et al.[61] It is based on the assumption that the available energy goes initially into the translation of Cl and C, which are considered independent from the rest of the molecule. Only after the dissociation this energy is redistributed in the molecular fragment. This simple model is appropriate for a direct dissociation, which is faster than energy redistribution in the molecule. The impulsive model yields an expectation value $\langle f_T \rangle$ = 36% for the total translational energy release. Considering that the geometry change in the molecular fragment during dissociation is neglected, the agreement with the experimental value is reasonable. It has been shown that impulsive (i.e. direct) C-Cl bond rupture will lead to a significant part of the excess energy ending up as CCl_2 rotation.[32]

Table 2: Experimental values for the CCl_2 fragments from CCl_3 photodissociation.

λ_{diss} /nm	$E_T^{max}(CCl_2)$ /eV	$\langle E_T \rangle$ /eV	$\langle f_T \rangle$ /%	β
230	0.75	0.21	28	0.50
235	0.72	0.19	26	0.20
240	0.68	0.19	28	0.13
245	0.65	0.19	29	0.05
250	0.62	0.17	27	0.06

As visible in Figure 5, there is a contribution at higher translational energies that extends beyond $\boldsymbol{E_T^{max}}$ and does not originate from channel (I). It is either the result of a background signal that could not be fully subtracted, from the dissociation of one of the higher masses visible in the mass spectrum, or from a small multiphoton contribution that is present, although a low laser power was used and the beam was not focused.

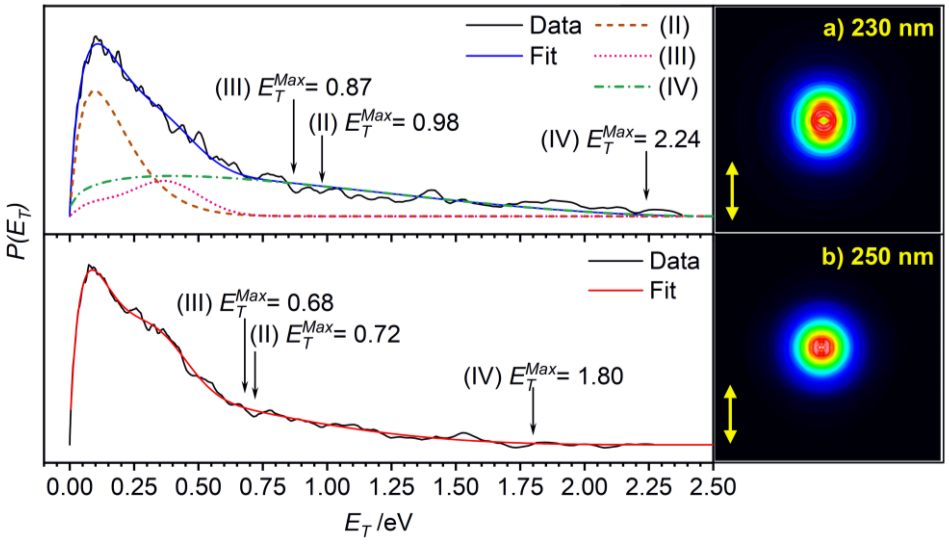

Figure 6: Translational energy distribution $P(E_T)$ of the CCl fragment using CCl_4 as a precursor. In a) 230 nm and in b) 250 nm light was used for dissociation. The experimental results are shown in black, while fits are shown in blue or red. In the upper trace the fit to the CCl_2 data obtained from Figure 7 (see below) is given as a dotted magenta line, assumed contributions from CCl_3 are given as a dashed brown line, while multiphoton contributions are given in green. The corresponding Velocity Map Images are shown with a yellow arrow indicating the laser polarisation. Again the translational energy of the CCl fragment is plotted on the abscissa, because $P(E_T)$ contains contributions from the photodissociation of CCl_3 and CCl_2.The red line in the bottom trace assumes similar components (scaled) at 250 nm.

The second pathway (II) for photodissociation of CCl_3 leads to CCl + Cl_2, therefore velocity map images of CCl were also recorded. However, as noted above CCl can also be formed from CCl_2 via (III) or (IV). Figure 6 shows $P(E_T)$ for a) 230 nm and b) 250 nm (black curve). Data at further wavelengths are given in Figure S5. Note again that E_T of the CCl fragment is plotted on the x-axis rather than the total translational energy release, because contributions from two different molecules (CCl_2 and CCl_3) have to be considered. A bi- or multimodal distribution is evident from the shape. The contributions to the fit will be discussed below. At 250 nm excitation, the distribution maximizes around 0.1 eV, followed by a shoulder at around 0.4 eV. Furthermore, a background signal is again present, which extends to high translational energies. Anisotropy is evident at 230 nm, but less pronounced at 250 nm. Data obtained at further dissociation wavelengths are given in Figure S5. The energy cut-offs for the various product channels are indicated by arrows. As visible, $P(E_T)$ extends beyond the limit given by reactions (II) and (III). $\boldsymbol{E_T^{max}}$ for the CCl fragment after dissociation with 230 nm light for reaction (III) is 0.87 eV, for reaction (II) 0.98 eV and for the consecutive two-photon process (IV) 2.24 eV. We thus conclude that the latter process (IV) is responsible for this contribution at large E_T. The maximum possible E_T values at the various excitation wavelengths are summarised in the ESI, Table S1.

Photofragment imaging of CCl_2 photodissociation. To get information on the possible presence of (II) to the $P(E_T)$ of CCl, we conducted experiments using $CHCl_3$ as a precursor, which is known to produce predominately CCl_2 upon pyrolysis (see mass spectra in Figure S1). Figure 7 shows the velocity map image of the CCl fragment after dissociation of CCl_2 with 230 nm light. Two contributions are discernible, an isotropic first one at low energies (around 0.1 eV) and a second one centred at around 0.4 eV, which is strongly anisotropic. Interestingly, the high energy component visible in Figure 6 is absent, supporting its assignment to (IV). Experimental conditions (mainly pyrolysis power) were varied in order to increase and decrease the amount of CCl_3 generated as a side product and additional VMIs were recorded. However, the two contributions in the CCl image did not change appreciably when the experimental conditions were changed. This confirms that both contributions belong to the dissociation of CCl_2. Its photodissociation dynamics has been investigated in detail by Dagdigian and co-workers, who monitored the CCl fragment by laser induced fluorescence,[15-17] and by Huber and coworkers, who employed photofragment translational spectroscopy (PTS).[18] The Dagdigian-group observed two different dissociation channels associated with different rotational state distributions of CCl. Thus, the two contributions obtained from the images are in qualitative agreement with this previous work. The isotropic contribution at low E_T in Figure 7 (dashed green line) is assumed to originate from a statistical process and a fit using function (1) yields $\langle E_T \rangle$ = 0.15 eV, corresponding to $\langle f_T \rangle$ = 17%. The high-energy contribution (dotted magenta line) is fitted by a Gaussian centred around $\langle E_T \rangle$=0.37 eV. Given that E_T^{Max} =0.87 eV, as indicated by the arrow in Figure 7, this corresponds to $\langle f_T \rangle$ = 43% released into translation of the CCl fragment. Taking the translational energy of the Cl counterfragment into account, an expectation value for the total translational energy release $\langle E_T \rangle_{tot}$ = 0.89 eV (86 kJ·mol^{-1}) is obtained. This process is associated with a β-value close to 1. Note that a more detailed study on the photodissociation dynamics of CCl_2 is currently underway. PTS at 248 nm yielded a comparable value of $\langle E_T \rangle_{tot} \approx$ 100 kJ·mol^{-1}, corresponding to roughly 1 eV, but only a negligible anisotropy was observed.[18]

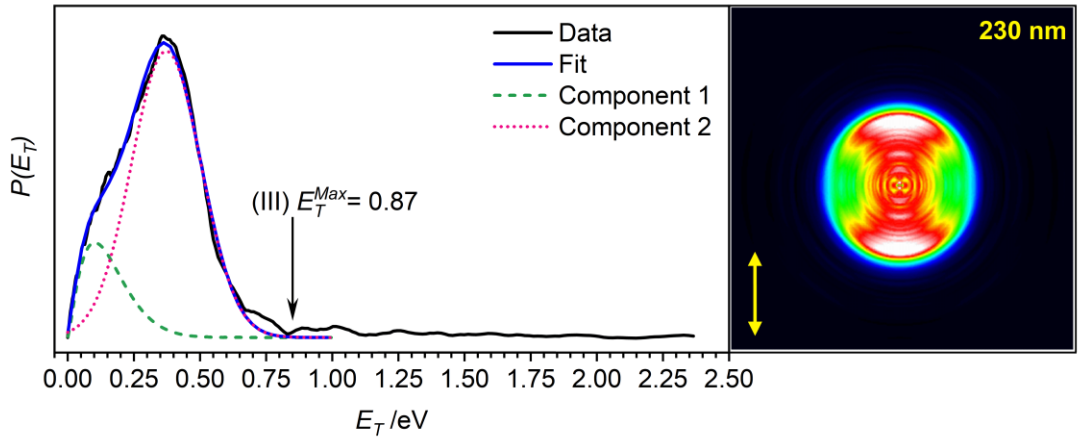

Figure 7: Translational energy distribution P(E_T) of CCl using $CHCl_3$ as a precursor and dissociating at 230 nm. The experimental results are shown in black, while a superposition of a two-parameter fit (expression (1)) and a Gaussian distribution is shown in blue. The individual functions are drawn in dashed lines. The corresponding velocity map images are shown with an arrow indicating the laser polarisation in yellow.

Going back to the photodissociation of CCl_3 in Figure 6, it is evident that the shoulder in trace b) at around 0.4 eV is due to the anisotropic component observed in reaction (III) for the photodissociation of CCl_2 (dotted magenta line). However, the low energy contribution is significantly more intense in Figure 6 than in Figure 7. Concluding from the contribution at large E_T, part of the signal at all E_T will be due to (IV), indicated as a dash-dotted green line, but there seems to be an additional component that appears exclusively at low E_T (dashed brown line). It suggests that reaction (II) occurs in CCl_3 as an additional contribution. The fit in the upper trace of figure 6 (full blue line) contains the various contributions. Note that due to the large number of free parameters, this fit represents only an approximation and should be considered with care. This is particularly true for the fit at 250 nm (red line), which employs a scaled CCl_2 distribution. As (II) is associated with Cl_2 formation, we also attempted to detect molecular chlorine via the REMPI line at 118.94 nm,[62] but were unsuccessful. This in turn seems to indicate that reaction (II) is of minor importance. However, it is hard to detect photofragments when the oscillator strength is distributed over a large number of transitions.

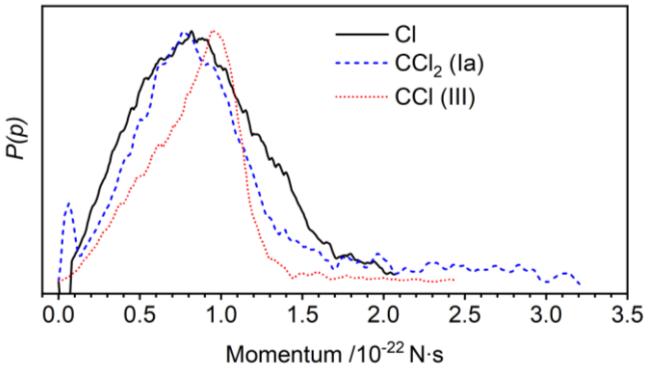

Figure 8: Translational energy distribution of atomic Cl (black) as a function of momentum, recorded at 230 nm. The blue dashed line shows the distribution expected from momentum-matching of the CCl_2 signal. The red dotted line indicates the momentum matching expected for a CCl co-fragment from the photodissociation of CCl_2 (III). As visible, the Cl and CCl fragments do not match well.

Chlorine Images. Further information on the dissociation dynamics should be available from the atomic fragment. Due to the large absorption cross section of CCl_3 at 230 nm, it is not possible to monitor Cl-atoms via [2+1] REMPI at 235 nm, because the focussing conditions cause multiphoton excitation of the radical. On the other hand, a [3+1] process at 356.7 nm did not yield analysable Cl images. As in previous work, we therefore resorted to ionisation of atomic Cl in a [1+1'] process via the $^2D_{5/2} \leftarrow {}^2P^o_{3/2}$ transition, using VUV excitation at 118.9 nm.[45] A velocity map image of the atomic chlorine $^2P_{3/2}$ fragment was recorded at a dissociation wavelength of 230 nm, using pyrolysis of CCl_4. It is given in Figure S7. As noted above, the spin-orbit excited $^2P_{1/2}$ state of Cl cannot be probed by this scheme. If the Cl atom and the CCl_2 fragment originate from the same process, the momenta calculated from the translational energy distributions of the two fragments should be matched with each other. The blue line in Figure 8 represents the expected Cl distribution momentum-matched with the CCl_2 distribution given in the upper trace of Figure 5, corresponding to reaction (I). As visible the maxima overlap quite well, indicating that the major part of the Cl atoms originates from process (Ia). However, the width of the distribution does not match and deviations at low and high momentum indicate that other processes contribute to the Cl-signal. Figure S8 illustrates P_2 as a function of momentum for CCl_2 and Cl. As visible, both follow the same trend, but for chlorine, P_2 is less pronounced and even becomes negative at momenta larger $1 \cdot 10^{-22}$ N·s. This confirms the existence of a further contribution at higher momenta that is not associated with photodissociation of CCl_3. The Cl distribution expected from reaction (III) is given as a red line in Figure 8. It should be rather narrow and centred at a slightly higher momentum, therefore it can only partially explain the deviations in the distribution. Therefore fragments produced from CCl_3 after multiphoton excitation via (IV) as well as chlorine-fragments from (V) might contribute to the Cl signal over a range of translational energies or momenta, respectively.

D Discussion

A model of the photodynamics of CCl_3 can be derived by combining the information from fs time-resolved PES with the information on the dissociation products, available from photofragment imaging with ns-lasers. While the former gives insight into the processes directly after excitation, the latter sheds light on the later steps of the photochemistry. It is important to keep in mind that CCl_3 is a rather complicated radical with a number of low-lying electronic states that has only scarcely been investigated. The description will therefore be less detailed than the one possible for diatomics or simple hydrocarbons.

In all experiments, the UV absorption band starting around 270 nm and previously observed by Ellerman is excited.[30] As evident from Table 1, the 1 ^2E, 2 ^2E and the 3 $^2A_1$ (3s) states lie close to each other and based on their computed oscillator strengths the latter two will contribute to this band, which has previously been assigned as 3 $^2A_1$ (3s). The electron kinetic energy in the TR-PES (cf. Figure 4) shows that single photon excitation dominates and that the red edge of the absorption band is excited. The excitation energy will be rapidly redistributed between these electronic states. The time constant of around 50 fs observed in the time-resolved spectra reflects the redistribution of energy and subsequent motion out of the Franck-Condon region. Furthermore, we expect rapid depopulation of the higher excited state and transfer of the molecule to the lower-lying states, most likely 2 $^2A_1$ and 1 $^2A_2$. Based on the data available for alkyl halides like CH_3Cl, [6, 63] and preliminary computations, these lower lying states are expected to be repulsive with respect to the C-Cl bond. As discussed above, a second time constant is evident in the time-domain data, but cannot be accurately determined. Its presence shows that the initial 50 fs process does not correspond to the time for dissociation. We assume that it reflects this nonradiative population transfer to the

lower-lying electronic states. One has to keep in mind that fs-experiments were conducted at a single excitation wavelength only. Time constants and initial dynamics might therefore change at higher excitation energies.

At first glance it might appear appropriate to compare CCl_3 with the methyl radical, CH_3. However, the latter is planar and the lowest-lying electronically excited states correspond to Rydberg-states. In contrast, the nonbonding *p*-orbitals on the chlorine atoms, n_{Cl} enforce a pyramidal geometry of CCl_3 and additional low-energy transitions due to excitation of these orbitals. Thus nonradiative deactivation pathways are available that are not present in methyl.

While TR-PES unravels the early steps of the dynamics, photofragment imaging gives information on the product state distributions, i.e. the processes that occur after the rapid population transfer to the lower-lying states. The ns-data show that reaction (I) dominates, i.e. loss of Cl, associated with CCl_2. As visible in Scheme 1, four pathways are possible for loss of a chlorine atom, leading to CCl_2 either in the X $^1A_1$ ground state or the a $^3B_1$ excited triplet state. Both can be formed with a Cl atom in the $^2P_{3/2}$ ground state or the $^2P_{1/2}$ spin-orbit excited state, which are separated by 10.52 kJ·mol^{-1}. The latter two cannot be distinguished in the translational energy distribution. Due to side reactions contributing to the Cl signal, most information on (I) is available when the CCl_2 molecular fragment is monitored.

Interpretation of the data and derivation of a dissociation model are not straightforward. The image shows a unimodal distribution, with the fraction of excess energy released into product translation $\langle f_T \rangle$ = 26-29%, assuming formation of CCl_2 in the X $^1A_1$ ground state (Ia). Formation of CCl_2 in the $a\ ^3B_1$ state (Ib) would also be thermochemically possible, but $P(E_T)$ extends beyond the maximum translational energy expected for this reaction, so the X $^1A_1$ product state has to dominate. For example, at 250 nm, the observed $\langle E_T \rangle$ would correspond to $\langle f_T \rangle \approx 60\%$ assuming a triplet product, far above the range expected for statistical as well as impulsive dissociation. In addition, $P(E_T)$ is unimodal and β does not vary with translational energy. Due to the radical temperature in the jet of 150 K (vide supra) hot band transitions might contribute, but especially at 250 nm excitation they cannot explain the shape of $P(E_T)$ when compared with previous work.[43, 64] Therefore, we assume that (Ia) dominates and contributions from (Ib) are small, if present at all. Formation of CCl_2 (A $^1B_1$) is energetically possible at the highest excitation energies, but not consistent with the observed $P(E_T)$. As the molecular fragment is monitored and the VUV detection scheme cannot probe Cl*, there is no information on the spin-orbit branching ratio. The shape of $P(E_T)$ appears Boltzmann-like and at first glance seems to indicate a ground state dissociation after redistribution of vibrational energy, following a statistical mechanism. However, 26-29% of the excess energy are released into translation, which is significantly more than usually observed in a statistical distribution. In the statistical photodissociation of cyclic hydrocarbons[64, 65] and aryl chlorides at 193 nm[66] values for $\langle f_T \rangle$ between 10% and 12% have been observed, while in the H-atom loss from hydrocarbon radicals $\langle f_T \rangle$ of up to 15 to 20% have been reported.[67, 68,]Thus in the present work $\langle f_T \rangle$ exceeds the range of values previously observed for statistical dissociation. In addition, an anisotropic PAD with a positive β is observed, which suggests that dissociation is faster than a rotational period and thus supports a model based on a direct dissociation According to preliminary computations, both the 2 $^2A_1$ and 1 $^2A_2$ states of CCl_3 result in a dissociation to the X $^1A_1$ state of CCl_2. Dissociation in these states would be commensurate with the observations. From an impulsive model for dissociation along a repulsive coordinate we expect a larger $\langle f_T \rangle$ = 0.36, but this simple approach neglects effects like geometry changes during the dissociation and should thus be seen as a limiting case. Interestingly, β decreases with an increase in wavelength from 0.5 at 230 nm to 0.06 at 250 nm (see Figure S6), suggesting either a slower dissociation at lower energies or an involvement of different electronic states. Different contributions of the 2 ^2E (D_4) and 3 $^2A_1$ (D_5) states to the initial absorption might lead to different anisotropies. As for the 2 ^2E state μ_T is oriented in the C-Cl plane, we expect a positive β-value for the Cl photofragment angular distribution, whereas for the (most likely planar) 3 $^2A_1$ state, a negative β is expected, because μ_T is oriented along the symmetry axis.[69] Therefore, the contribution of the 2 ^2E state to the absorption band might increase to the blue and possibly lead to a change of dissociation mechanism with excitation energy. However, the almost constant shape of $P(E_T)$ at all wavelengths does not support this model. We therefore suggest an alternative explanation, a stepwise deactivation of the optically excited state. At lower excitation energies, CCl_3 could be trapped for a few vibrational periods in an intermediate state (e.g. the 1 $^2A_2$), sufficiently long to partially lose its anisotropy, whereas at higher excitation energies such a barrier is rapidly surmounted. Note that the rise time of the two-colour signal (Figure S3) is on the scale of the laser pulse duration, in agreement with a dissociation on a subns time scale. High-level computations are required to verify this model.

The only previous study on CCl_3 photodissociation was reported by Hintsa et al, who excited the radical at 308 nm and observed the CCl_2 fragment by translational energy spectroscopy. [32] Here, CCl_3 was generated by photolysis of CCl_4 at 193 nm, so radicals were most likely internally hot. Hintsa et al observed a total translational energy release of less than 30% and β=1.0±0.2, in qualitative agreement with the present results. No indication of pathway (II), loss of Cl_2 was found in this work.

Besides the CCl_2 molecular fragment, the Cl signal has also been analysed at 230 nm. Momentum matching of CCl_2 and Cl fragments and a comparable anisotropy parameter β indicate that both fragments predominately originate from the same source. However, there are visible differences that suggest contributions from competing processes to the Cl signal, possibly dissociation of CCl_2 (III) or CCl_4 (V) as well as multiphoton-processes (IV), so it is difficult to disentangle their contribution from (I).

In addition to Cl-loss, pathway (II) to CCl + Cl_2 is also thermochemically accessible (see Scheme 1). The CCl images show two distinguishable features, a dominant low energy one, which

maximizes at around 0.1 eV and a second one centred around 0.4 eV. However, CCl_2, which is a minor product in the pyrolysis can also dissociate to CCl (see right-hand side of Scheme 1). Control experiments using $CHCl_3$, a known precursor for CCl_2, also yield a bimodal translational energy distribution for the CCl photofragment. The higher energy component, centred at 0.4 eV is dominant in the experiments utilizing $CHCl_3$ and can thus be assigned to pathway (III), photodissociation of CCl_2 produced in the pyrolysis to CCl + Cl. The anisotropic PAD for this main peak with β between 0.7 and 1 and the large $\langle f_T \rangle$ of about 43% indicate that CCl_2 dissociates to CCl along a repulsive coordinate. An impulsive model yields $\langle f_T \rangle$=0.41, in almost perfect agreement with the experiment. The origin of a low energy contribution in the photodissociation of CCl_2 is still being investigated, but the smaller $\langle f_T \rangle$ and the absence of anisotropy point towards a statistical mechanism. With this information, the peaks in the CCl image from CCl_4 as a precursor can be assigned. The distribution derived from the CCl_2 experiment is given as a dotted magenta line in the upper trace of Figure 6 (230 nm dissociation). The shoulder at around 0.4 eV is attributed to the direct dissociation of CCl_2 formed in the pyrolysis and not related to CCl_3 photodissociation. However, the low energy contribution at around 0.1 eV is significantly larger than in the CCl_2 experiments, thus it seems to originate partially from CCl_3 dissociation. This additional contribution at low energy is depicted as a dashed brown line in the figure. The $P(E_T)$ of CCl also shows a signal that extends to high translational energies and requires absorption of two photons. This component must originate from the consecutive process (IV), which deposits extra internal energy in the CCl_2 and thus leads to a broad $P(E_T)$. It is indicated as a dash-dotted green line in the Figure. It is difficult to imagine that the strong component maximizing at E_T =0.1 eV is exclusively due to this sequential process. Thus we conclude that reaction (II) contributes to this component, represented as a dashed brown line in Figure 6. We point out that the counter-fragment Cl_2 has not been detected. Quantification of the various reaction channels is not possible, because the ionisation cross sections σ_{ion} of CCl_2 and CCl are not known. Compared to alkyl chlorides, one important difference should be noted. In many alkyl halides, the spin orbit branching ratio of chlorine is determined by the interaction between the $^3Q_0$ and the ^1Q states. In CCl_3, however, all low-lying excited states are doublets, with the quartet states higher in energy. Direct dissociation of a quartet state corresponds to a CCl_2 fragment either in the triplet (Ib) or the open-shell singlet state. The present work provides no evidence for either product and thus rules out dissociation from a quartet state. Nevertheless, quartet states might be involved in the non-radiative relaxation. The question of whether such interactions lead to the formation of spin-orbit excited chlorine atoms remains open.

Conclusions

The photodissociation dynamics of CCl_3 upon UV excitation was investigated by fs time-resolved photoionisation and photofragment imaging of the reaction products to follow the photodynamics along the complete reaction coordinate. The radical was generated by pyrolysis of CCl_4 and CH_3Br. Excitation between 230 nm and 266 nm is due to transitions into the D_4 (^2E) and D_5 ($^2A_1$) states, as indicated by TD-DFT. The fs-experiments show a rapid motion out of the Franck-Condon window within around 50 fs. A second slightly longer time constant is recognisable, but cannot be determined accurately. It is most likely due to a fast nonradiative deactivation to lower-lying dissociative electronic states. Here, the fate of the radicals was monitored by photofragment imaging. Dissociation of CCl_3 leads to CCl_2 + Cl. A velocity map image of the CCl_2 photofragment shows an anisotropic distribution and a translational energy release of 26-29%, indicating a dissociation in less than a rotational period. The Cl-fragment image is to a large extent momentum matched and the β-parameter is similar, but it contains additional contributions, in part from the photodissociation of CCl_2, which is produced in the pyrolysis in small amounts. Furthermore, as the photoproduct from CCl_3 it can absorb a second photon and dissociate.

Images of CCl were recorded to get insight into the second reaction pathway, leading to CCl + Cl_2. Control experiments using the pyrolysis of CH_3Cl, a known CCl_2 precursor, revealed the contribution of CCl_2 dissociation to the CCl fragment signal. An anisotropic component centred at around 0.4 eV is due to direct dissociation of CCl_2. An isotropic one at low translational energies increases significantly when CCl_3 is present, indicating the presence of reaction (II), dissociation of CCl_3 to CCl + Cl_2. The long tail in the translational energy distribution shows the presence of a multiphoton process, i.e. stepwise dissociation of CCl_3, thus the CCl contribution that originates from (II) cannot be quantified.

Acknowledgements

This work has been financially supported by the Deutsche Forschungsgemeinschaft, GRK 2112 and FI 575/13-1. The femtosecond experiments were conducted at the CEA Saclay and supported by Laserlab Europe (SLIC001972). We would like to thank Jens Giegerich for contributions to the fs-experiments. Travel support by the DAAD and by PHC Program PROCOPE 2015 (Grant No. 32980XH) is gratefully acknowledged. The authors kindly thank Michel Perdrix and Delphine Guillaumet for setting up and maintaining the SLIC/LUCA laser. A.R. thanks Ryan E. McDonell for helpful and insightful discussions.

Notes and references

‡ Bromine has an IE of 11.81 eV. Ionisation via a [1+5'] or [2+2'] process with a total energy of 12.41 eV would be in agreement with eKE≈0.5 eV, assuming a non-perfect energy calibration. However, an alternative origin might be the dissociative photoionisation of Br_2 formed in the pyrolysis reactor in a [1+4'] process, AE(Br^+, B_2)=10.48 eV.

1. M. J. Molina and F. S. Rowland, *Nature*, 1974, **249**, 810.
2. T. L. Myers, D. C. Kitchen, B. Hu and L. J. Butler, *J. Chem. Phys.*, 1996, **104**, 5446.

3. M. L. Morton, L. J. Butler, T. A. Stephenson and F. Qi, *J. Chem. Phys.*, 2002, **116**, 2763.
4. Y. Matsumi, P. K. Das and M. Kawasaki, *J. Chem. Phys.*, 1992, **97**, 5261.
5. Y. Matsumi, P. K. Das and M. Kawasaki, *J. Chem. Phys.*, 1990, **92**, 1696.
6. J. J. Lin, Y. Chen, Y. Y. Lee, Y. T. Lee and X. M. Yang, *Chem. Phys. Lett.*, 2002, **361**, 374.
7. C. D. Foley, B. Joalland, S. T. Alavi and A. G. Suits, *Phys Chem Chem Phys*, 2018, **20**, 27474.
8. S. Deshmukh and W. P. Hess, *J. Chem. Phys.*, 1994, **100**, 6429.
9. M. Ahmed, D. S. Peterka, P. Regan, X. H. Liu and A. G. Suits, *Chem. Phys. Lett.*, 2001, **339**, 203.
10. R. N. Dixon and H. W. Kroto, *Trans. Faraday Soc.*, 1963, **59**, 1484.
11. G. Herzberg, *Molecular Spectra and Molecular Structure. I. Spectra of Diatomic Molecules*, Krieger, Malabar/FL, 1989.
12. V. E. Bondybey, *J. Mol. Spectrosc.*, 1977, **64**, 180.
13. C. Richmond, C. Tao, C. Mukarakate, H. Fan, K. Nauta, T. W. Schmidt, S. H. Kable and S. A. Reid, *J. Phys. Chem. A*, 2008, **112**, 11355.
14. M. L. Liu, C. L. Lee, A. Bezant, G. Tarczay, R. J. Clark, T. A. Miller and B. C. Chang, *Phys. Chem. Chem. Phys.*, 2003, **5**, 1352.
15. S. K. Shin and P. J. Dagdigian, *J. Chem. Phys.*, 2008, **128**.
16. S. K. Shin and P. J. Dagdigian, *J. Chem. Phys.*, 2006, **125**.
17. S. K. Shin and P. J. Dagdigian, *Phys. Chem. Chem. Phys.*, 2006, **8**, 3446.
18. G. P. Morley, P. Felder and J. R. Huber, *Chem. Phys. Lett.*, 1994, **219**, 195.
19. G. B. Bacskay, *Mol. Phys.*, 2015, **113**, 1608.
20. C. Tao, C. Richmond, C. Mukarakate, R. Dawes, S. H. Kable and S. A. Reid, *J. Chem. Phys.*, 2011, **135**.
21. C. Tao, C. Mukarakate and S. A. Reid, *J. Mol. Spectrosc.*, 2007, **241**, 136.
22. R. Schlachta, G. Lask, A. Stangassinger and V. E. Bondybey, *J. Phys. Chem.*, 1991, **95**, 7132.
23. T. E. Mogelberg, J. Sehested, O. J. Nielsen and T. J. Wallington, *J. Phys. Chem.*, 1995, **99**, 16932.
24. A. A. Gushchin, V. I. Grinevich, T. V. Izvekova, E. Y. Kvitkova, K. A. Tyukanova and V. V. Rybkin, *Chemosphere*, 2021, **270**.
25. W. C. Nottingham and R. N. Rudolph, *Int. J. Chem. Kin.*, 1994, **26**, 749.
26. F. F. Fenter, P. D. Lightfoot, J. T. Niiranen and D. Gutman, *J. Phys. Chem.*, 1993, **97**, 5313.
27. F. Danis, F. Caralp, M. T. Rayez and R. Lesclaux, *J. Phys. Chem.*, 1991, **95**, 7300.
28. J. W. Hudgens, R. D. Johnson, B. P. Tsai and S. A. Kafafi, *J. Am. Chem. Soc.*, 1990, **112**, 5763.
29. F. Danis, F. Caralp, B. Veyret, H. Loirat and R. Lesclaux, *Int. J. Chem. Kin.*, 1989, **21**, 715.
30. T. Ellermann, *Chem. Phys. Lett.*, 1992, **189**, 175.
31. E. S. J. Robles and P. Chen, *J. Phys. Chem.*, 1994, **98**, 6919.
32. E. J. Hintsa, X. S. Zhao, W. M. Jackson, W. B. Miller, A. M. Wodtke and Y. T. Lee, *J. Phys. Chem.*, 1991, **95**, 2799.
33. M. Horn and P. Botschwina, *Chem. Phys. Lett.*, 1994, **228**, 259.
34. A. Röder, J. Petersen, K. Issler, I. Fischer, R. Mitric and L. Poisson, *J. Phys. Chem. A*, 2019, **123**, 10643.
35. A. Stolow, A. E. Bragg and D. M. Neumark, *Chem. Rev.*, 2004, **104**, 1719.
36. A. Stolow, *Annu. Rev. Phys. Chem.*, 2003, **54**, 89.
37. A. T. J. B. Eppink and D. H. Parker, *Rev. Sci. Instrum.*, 1997, **68**, 3477.
38. B. J. Whitaker, ed., *Imaging in Molecular Dynamics*, Cambridge University Press, Cambridge, 2003.
39. C. Vallance, *Chem. Commun.*, 2019, **55**, 6336.
40. A. G. Suits, *Rev. Sci. Instrum.*, 2018, **89**.
41. M. N. R. Ashfold, R. A. Ingle, T. N. V. Karsili and J. S. Zhang, *Phys. Chem. Chem. Phys.*, 2019, **21**, 13880.
42. M. Steinbauer, J. Giegerich, K. H. Fischer and I. Fischer, *J. Chem. Phys.*, 2012, **137**, 014303.
43. J. Giegerich, I. Fischer, J. Petersen and R. Mitric, *Phys. Chem. Chem. Phys.*, 2014, **16**, 6294.
44. M. S. Schuurman, J. Giegerich, K. Pachner, D. Lang, B. Kiendl, R. J. MacDonell, A. Krueger and I. Fischer, *Chem. Eur. J.*, 2015, **21**, 14486.
45. C. T. Matthaei, D. P. Mukhopadhyay and I. Fischer, *J Phys Chem A*, 2021, **125**, 2816.
46. A. Röder, K. Issler, L. Poisson, A. Humeniuk, M. Wohlgemuth, M. Comte, F. Lepetit, I. Fischer, R. Mitric and J. Petersen, *J. Chem. Phys.*, 2017, **147**.
47. A. Röder, A. Humeniuk, J. Giegerich, I. Fischer, L. Poisson and R. Mitric, *Phys. Chem. Chem. Phys.*, 2017, **19**, 12365.
48. G. A. Garcia, L. Nahon and I. Powis, *Rev. Sci. Instrum.*, 2004, **75**, 4989.
49. Y. H. Shao, Z. T. Gan, E. Epifanovsky, A. T. B. Gilbert, M. Wormit, J. Kussmann, A. W. Lange, A. Behn, J. Deng, X. T. Feng, D. Ghosh, M. Goldey, P. R. Horn, L. D. Jacobson, I. Kaliman, R. Z. Khaliullin, T. Kus, A. Landau, J. Liu, E. I. Proynov, Y. M. Rhee, R. M. Richard, M. A. Rohrdanz, R. P. Steele, E. J. Sundstrom, H. L. Woodcock, P. M. Zimmerman, D. Zuev, B. Albrecht, E. Alguire, B. Austin, G. J. O. Beran, Y. A. Bernard, E. Berquist, K. Brandhorst, K. B. Bravaya, S. T. Brown, D. Casanova, C. M. Chang, Y. Q. Chen, S. H. Chien, K. D. Closser, D. L. Crittenden, M. Diedenhofen, R. A. DiStasio, H. Do, A. D. Dutoi, R. G. Edgar, S. Fatehi, L. Fusti-Molnar, A. Ghysels, A. Golubeva-Zadorozhnaya, J. Gomes, M. W. D. Hanson-Heine, P. H. P. Harbach, A. W. Hauser, E. G. Hohenstein, Z. C. Holden, T. C. Jagau, H. J. Ji, B. Kaduk, K. Khistyaev, J. Kim, J. Kim, R. A. King, P. Klunzinger, D. Kosenkov, T. Kowalczyk, C. M. Krauter, K. U. Lao, A. D. Laurent, K. V. Lawler, S. V. Levchenko, C. Y. Lin, F. Liu, E. Livshits, R. C. Lochan, A. Luenser, P. Manohar, S. F. Manzer, S. P. Mao, N. Mardirossian, A. V. Marenich, S. A. Maurer, N. J. Mayhall, E. Neuscamman, C. M. Oana, R. Olivares-Amaya, D. P. O'Neill, J. A. Parkhill, T. M. Perrine, R. Peverati, A. Prociuk, D. R. Rehn, E. Rosta, N. J. Russ, S. M. Sharada, S. Sharma, D. W. Small, A. Sodt, T. Stein, D. Stuck, Y. C. Su, A. J. W. Thom, T. Tsuchimochi, V. Vanovschi, L. Vogt, O. Vydrov, T. Wang, M. A. Watson, J. Wenzel, A. White, C. F. Williams, J. Yang, S. Yeganeh, S. R. Yost, Z. Q. You, I. Y. Zhang, X. Zhang, Y. Zhao, B. R. Brooks, G. K. L. Chan, D. M. Chipman, C. J. Cramer, W. A. Goddard, M. S. Gordon, W. J. Hehre, A. Klamt, H. F. Schaefer, M. W. Schmidt, C. D. Sherrill, D. G. Truhlar, A. Warshel, X. Xu, A. Aspuru-Guzik, R. Baer, A. T. Bell, N. A. Besley, J. D. Chai, A. Dreuw, B. D. Dunietz, T. R. Furlani, S. R. Gwaltney, C. P. Hsu, Y. S. Jung, J. Kong, D. S. Lambrecht, W. Z. Liang, C. Ochsenfeld, V. A. Rassolov, L. V. Slipchenko, J. E. Subotnik, T. Van Voorhis, J. M. Herbert, A. I. Krylov, P. M. W. Gill and M. Head-Gordon, *Mol Phys*, 2015, **113**, 184.

50. L. Barnes, S. Abdul-Al and A.-R. Allouche, *J. Phys. Chem. A*, 2014, **118**, 11033.
51. D. W. Kohn, E. S. J. Robles, C. F. Logan and P. Chen, *J. Phys. Chem.*, 1993, **97**, 4936.
52. B. Ruscic and D. H. Bross, Active Thermochemical Tables (ATcT) values based on ver. 1.122p of the Thermochemical Network, ATcT.anl.gov).
53. B. Ruscic, R. E. Pinzon, M. L. Morton, G. von Laszevski, S. J. Bittner, S. G. Nijsure, K. A. Amin, M. Minkoff and A. F. Wagner, *J. Phys. Chem. A*, 2004, **108**, 9979.
54. H. Keller-Rudek, G. K. Moortgat, R. Sander and R. Sörensen, *Earth Syst. Sci. Data*, 2013, **5**, 365.
55. M. Kawasaki, K. Suto, Y. Sato, Y. Matsumi and R. Bersohn, *J. Phys. Chem.*, 1996, **100**, 19853.
56. R. E. Rebbert and P. J. Ausloos, *J. Photochem.*, 1976/77, **6**, 265.
57. K. Pachner, M. Steglich, P. Hemberger and I. Fischer, *J. Chem. Phys.*, 2017, **147**, 084303.
58. H. J. Deyerl, I. Fischer and P. Chen, *J. Chem. Phys.*, 1999, **111**, 3441.
59. S. W. North, A. J. Marr, A. Furlan and G. E. Hall, *J. Phys. Chem. A*, 1997, **101**, 9224.
60. A. F. Tuck, *J Chem Soc Farad T 2*, 1977, **73**, 689.
61. D. B. Galloway, T. Glenewinkel-Meyer, J. A. Bartz, L. G. Huey and F. F. Crim, *J. Chem. Phys.*, 1994, **100**, 1946.
62. L. C. Lee, M. Suto and K. Y. Tang, *J. Chem. Phys.*, 1986, **84**, 5277.
63. H. M. Lambert and P. J. Dagdigian, *Chem. Phys. Lett.*, 1997, **275**, 499.
64. J. Giegerich and I. Fischer, *Phys. Chem. Chem. Phys.*, 2013, **15**, 13162.
65. K. Tsukiyama and R. Bersohn, *J. Chem. Phys.*, 1987, **86**, 745.
66. T. Ichimura, Y. Mori, H. Shinohara and N. Nishi, *J. Chem. Phys.*, 1997, **107**, 835.
67. J. Giegerich and I. Fischer, *J. Chem. Phys.*, 2015, **142**, 044304.
68. G. Sun, M. Lucas, Y. Song, J. Zhang, C. Brazier, P. L. Houston and J. M. Bowman, *J. Phys. Chem. A*, 2019, **123**, 9957.
69. T. P. Rakitzis and R. N. Zare, *J. Chem. Phys.*, 1999, **110**, 3341.

TOC Figure:

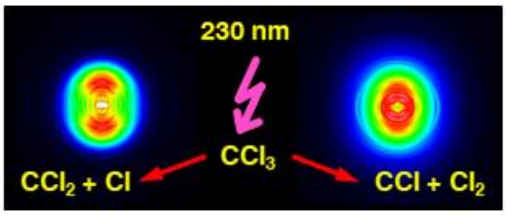

The photodissociation dynamics of CCl_3 has been investigated by femtosecond photoelectron and nanosecond photofragment spectroscopy, using velocity map imaging.